ACS Biomaterials SCIENCE & ENGINEERING

pubs.acs.org/journal/abseba

Article

Evaluation of the Immune Response to Chitosan-*graft*-poly(caprolactone) Biopolymer Scaffolds

Matthew J. Moore, Yuen Ting Lam, Miguel Santos, Richard P. Tan, Nianji Yang, Juichien Hung, Zihao Li, Kristopher A. Kilian, Jelena Rnjak-Kovacina, Johannes B. Pitts, Henning Menzel, and Steven G. Wise*

Cite This: https://doi.org/10.1021/acsbiomaterials.3c00553

Read Online

ACCESS | Metrics & More | Article Recommendations | Supporting Information

ABSTRACT: Biomimetic scaffolds recreating key elements of the architecture and biological activity of the extracellular matrix have enormous potential for soft tissue engineering applications. Combining appropriate mechanical properties with select biological cues presents a challenge for bioengineering, as natural materials are most bioactive but can lack mechanical integrity, while synthetic polymers have strength but are often biologically inert. Blends of synthetic and natural materials, aiming to combine the benefits of each, have shown promise but inherently require a compromise, diluting down favorable properties in each polymer to accommodate the other. Here, we electrospun a material comprising chitosan, a natural polysaccharide, and polycaprolactone (PCL), one of the most widely studied synthetic polymers used in materials engineering. In contrast to a classical blend, here PCL was chemically grafted onto the chitosan backbone to create chitosan-*graft*-polycaprolactone (CS-*g*-PCL) and then combined further with unmodified PCL to generate scaffolds with discreet chitosan functionalization. These small amounts of chitosan led to significant changes in scaffold architecture and surface chemistry, reducing the fiber diameter, pore size, and hydrophobicity. Interestingly, all CS-*g*-PCL-containing blends were stronger than control PCL, though with reduced elongation. In in vitro assessments, increasing the CS-*g*-PCL content led to significant improvements in in vitro blood compatibility compared to PCL alone while increasing fibroblast attachment and proliferation. In a mouse subcutaneous implantation model, a higher CS-*g*-PCL content improved the immune response to the implants. Macrophages in tissues surrounding CS-*g*-PCL scaffolds decreased proportionately to the chitosan content by up to 65%, with a corresponding decrease in pro-inflammatory cytokines. These results suggest that CS-*g*-PCL is a promising hybrid material comprising natural and synthetic polymers with tailorable mechanical and biological properties, justifying further development and in vivo evaluation.

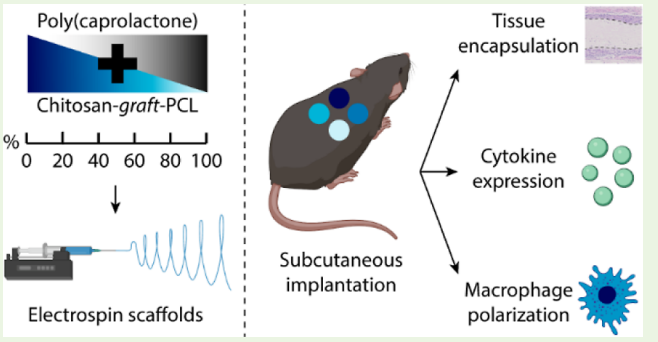

KEYWORDS: *chitosan, polycaprolactone, electrospinning, foreign body response, cell compatibility*

INTRODUCTION

Polycaprolactone (PCL) is one of the most common synthetic polymers used for biomedical applications. Its popularity stems from its high mechanical strength and relatively slow degradation rate, in the order of many months to years.[1,2] PCL is generally well tolerated in vivo and is compatible with various manufacturing techniques that allow it to be formed into a range of shapes and architectures.[3,4] In particular, PCL is one of the best-characterized polymers used to manufacture small-diameter vascular grafts other than clinically used ePTFE and Dacron. Detailed, longitudinal studies in both small and large animal models demonstrate that PCL grafts can support some local cell growth and tissue remodeling, especially as they degrade.[5−7] However, PCL is highly hydrophobic and lacks cell signaling motifs, leaving it biologically inert and resulting in suboptimal integration with the surrounding vascular tissue.[8]

An emerging strategy to improve the bioactivity of PCL is to blend it with naturally derived biomaterials.[9,10]

Natural materials possess intrinsic bioactivity that can be leveraged to improve the biocompatibility and functionality of tissue engineering scaffolds.[11] Among natural materials, chitosan, a linear polysaccharide derived from the deacetylation of chitin and a structural component of fungi cell walls and arthropod exoskeletons, offers several unique advantages. It possesses broad-spectrum antimicrobial and antifungal activ-

Received: April 28, 2023
Accepted: May 8, 2023

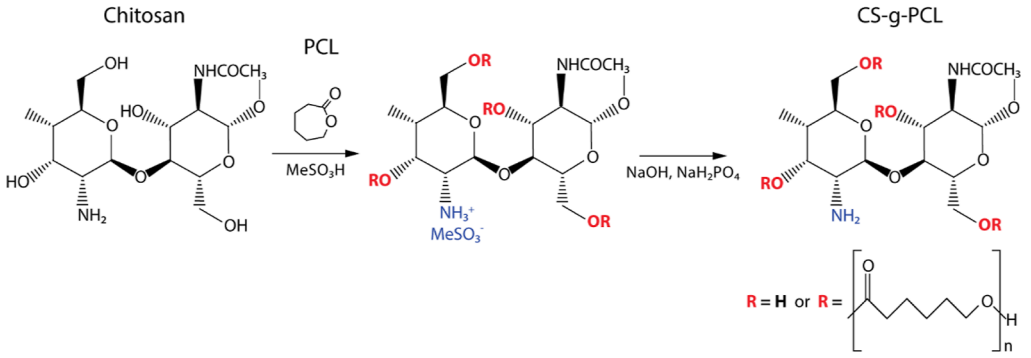

Figure 1. Chemical synthesis of chitosan-*graft*-poly(caprolactone) (CS-*g*-PCL). PCL is bonded to chitosan in a ring opening polymerization reaction to produce CS-*g*-PCL.

ities that can prevent infection, making it well studied for wound healing applications.[12,13] Additionally, chitosan has anti-inflammatory properties while also promoting cell adhesion and proliferation.[14,15] Combined with innocuous degradation products, chitosan is generally well tolerated in vivo.[16,17] The free primary amine groups present on the chitosan backbone also readily facilitate surface modification and give chitosan a net positive charge that improves cell adhesion.[18] Despite these appealing qualities, chitosan in its pure form is insoluble in many organic solvents, making it difficult to process for materials applications (e.g., by electrospinning), often forming hard, brittle scaffolds that handle poorly and are unsuited for soft tissue implantation.[19,20]

Chitosan-*graft*-poly(caprolactone) (CS-*g*-PCL) is a hybrid bio-synthetic copolymer developed to combine the best features of each constituent: the biological advantages of chitosan, with the mechanical strength and manufacturing ease of polycaprolactone (PCL). The CS-*g*-PCL copolymer is produced by grafting PCL to the hydroxyl groups present on the backbone of chitosan in a ring-opening polymerization reaction.[21,22] CS-*g*-PCL has been proposed as a scaffold material for engineering bone, skin, myocardium, and retinal tissues with promising in vitro findings, suggesting beneficial physical and biological properties.[20,23−25] Studies of electrospun PCL fibers (fiber width ∼ 2 μm), dip-coated in CS-*g*-PCL with similar underlying architecture demonstrate that the presence of CS-*g*-PCL strikingly reduced hydrophobicity and improved cell adhesion and in vivo vascularization.[26,27] These promising findings justify more detailed in vivo evaluation.

Here, we report the comprehensive in vitro and in vivo evaluation of scaffolds electrospun from blends of CS-*g*-PCL, comparing them to PCL alone. Production parameters, including electrospinning solvent, volume, flow rate, and concentration, were kept constant, but resulted in scaffolds with significant physical and chemical changes. We aimed to characterize the effects of increasing CS-*g*-PCL content on physical and mechanical properties, cell and blood interactions, and, for the first time, the immune response to subcutaneously implanted scaffolds.

MATERIALS AND METHODS

Materials. All reagents and materials were purchased from Sigma-Aldrich (St. Louise, MO, USA) and used as received unless otherwise specified. All antibodies were purchased from Abcam (Cambridge, United Kingdom).

Scaffold Fabrication. The CS-*g*-PCL copolymer was synthesized by bonding PCL to the hydroxyl groups of the chitosan backbone in a ring-opening polymerization reaction (Figure 1). In a typical reaction procedure, vacuum-dried chitosan and $MeSO_3H$ were stirred at 45 °C for 30 min to dissolve the chitosan, followed by the addition of the distilled ε-caprolactone monomer. The reaction mixture was stirred at 45 °C under nitrogen atmosphere for 5 h and then transferred into a solution containing 0.2 M KH_2PO_4, 10 M NaOH, and 100 g of crushed ice. The resulting CS-PCL (1:12) copolymer was collected by a vacuum filter and washed with deionized water several times until the pH reached 7.[21,22] According to ^{1}H-analysis, the ratio of chitosan to PCL was such that the average PCL side chain length was 24 units per glucosamine unit of chitosan. Six polymer solutions were created by dissolving CS-*g*-PCL and PCL (80,000 MW, Sigma-Aldrich) in ratios (w/w) of 0:100, 20:80, 40:60, 60:40, 80:20, and 100:0. Blends were dissolved in 1,1,1,3,3,3 hexafluoro-isopropanol (HFP) at 10% w/v by rotation overnight. Scaffold sheets were electrospun (IME Medical Electrospinning, Waalre, Netherlands) by infusing solutions at 1 mL/h with a syringe pump (11 Elite Series, Harvard Apparatus, Holliston, MA, USA) through a positively charged needle (0.6 mm Ø, 18 kV) toward a grounded, rotating mandrel (20 mm Ø, 500 rpm) positioned 200 mm from the needle. The electrospinner was contained in a climate-controlled cabinet (21 °C, 30% relative humidity). Scaffolds were cut from the mandrel along the long axis and crosslinked in glutaraldehyde vapor to stabilize the materials by placing in a vacuum chamber with 3 mL of 25% glutaraldehyde for 18 h at room temperature. To remove residual glutaraldehyde, scaffolds were soaked in ultrapure water overnight and air dried for one week.

Sample Preparation. Unless otherwise described, immediately prior to experimentation, samples were cut from electrospun scaffolds with a Stiefel 6 mm diameter circular biopsy punch, UV sterilized for 30 min on each side, and washed three times in sterile phosphate buffered saline (PBS; pH 7.4). Sterility was maintained until scaffolds were used.

Scanning Electron Microscopy. Samples were prepared for scanning electron microscopy (SEM) by gold sputter deposition (CCU-010 HV, Safematic, Zizers, Switzerland) under an argon atmosphere to a surface thickness of 15 nm. SEM was performed with a Zeiss Sigma VP HD field emission gun−SEM (Carl Zeiss AG, Jena, Germany) under high vacuum at an accelerating voltage of 5 kV. Contrast and brightness were constant for each micrograph. Four micrographs of each blend were taken at random locations.

Structural Characterization of CS-*g*-PCL/PCL Scaffolds. Fiber diameter, planimetric pore size, and porosity were assessed from SEM micrographs with ImageJ software (version 1.52r) using established methods.[28] Fiber diameter was estimated using the line segment tool to measure the cross-sectional thickness of 10 randomly chosen fibers in each micrograph (total n = 40). To estimate average planimetric pore size and porosity, micrographs were converted to binary images using a constant threshold, and particle analysis was used to measure areas > 0.1 μm^2 regardless of circularity. Pore size was calculated as the average of individual two-dimensional pore areas at the surface plane of each micrograph (n = 4 micrographs). Porosity was calculated as the fraction of total void area at the surface plane represented as a percentage of the field of view in each micrograph (n = 4 micrographs).

https://doi.org/10.1021/acsbiomaterials.3c00553
ACS Biomater. Sci. Eng. XXXX, XXX, XXX−XXX

Fourier Transform Infrared Spectroscopy. The infrared spectra of CS-*g*-PCL/PCL scaffolds were determined by Fourier transform spectroscopy in attenuated total reflectance mode (FTIR-ATR) using a Bruker Alpha spectrometer (Billerica, MA, USA). Each infrared spectrum was collected by averaging a total of 64 scans at a spectral resolution of 4 cm^{-1} within the wavenumber range of 800−4000 cm^{-1}. Spectral subtraction and baseline were applied using the OPUS software (Bruker, v7.5) to eliminate the background signal.

Water Contact Angle Measurements. The water contact angle (WCA) was measured using the sessile drop method, as previously described.[29] For each scaffold, 5 μL of deionized water was dropped onto the sample, images of static droplets were taken with a contact angle goniometer (ramé-hart, Succasunna, NJ, USA), and the angle between the edge of the water droplet and the surface was measured. A WCA of >90° was considered indicative of poor material wettability and hydrophobicity and <90° of hydrophilicity.[30] The mean WCAs for three droplets per blend were recorded.

Mechanical Properties. Mechanical properties were investigated by uniaxial tensile testing performed on an Instron model 5543 (Instron, Melbourne, Australia) equipped with a 50 N load cell. Samples were prepared by cutting rectangular strips from electrospun sheets 1 mm wide with a gauge length of 3 mm. Dimensions were confirmed with digital calipers prior to testing. Samples were hydrated for 1 h in PBS at 37 °C, and testing was conducted in a PBS bath at 37 °C. Force was applied by a constant crosshead speed of 10 mm/min until sample failure. Force and extension were recorded by Bluehill 2 software (version 2.15) and converted to engineering stress (eq 1) and strain (eq 2).

$$\text{Stress}(\sigma) = \frac{\text{force(N)}}{\text{area}(\text{m}^2)} \tag{1}$$

$$\text{Strain}(\epsilon) = \frac{\Delta\text{length}}{\text{length}} \tag{2}$$

Young's modulus was estimated from the gradient of stress−strain curves between a strain of 0.1−0.2 using linear regression. Ultimate tensile strength (UTS) was taken from the maximum stress recorded before failure. Elongation was calculated as the percent increase in length of the sample at failure compared to the gauge length. Four replicates per blend were tested.

Thrombogenicity. Approval for this work was granted by the University of Sydney Human Research Ethics Committee (protocol 05-2009/11668). Human whole blood was obtained from healthy, non-smoking male volunteers who had not consumed medication two weeks prior to donation with informed consent in accordance with the Declaration of Helsinki. Blood was collected by venipuncture with a 21-gauge butterfly needle in a polypropylene tube and heparinized (0.5 U/mL). All assays were started with minimal delay (<30 min) after blood collection. All assays were performed in 24-well plates using scaffold cut into 0.8 × 1.2 cm rectangles. Each well was pre-coated with 3% w/v bovine serum albumin (BSA) in PBS. Thrombogenicity was assessed by static whole blood and fibrinogen adhesion. To assess whole blood adhesion, scaffolds were pre-weighed and placed flat at the bottom of each well; then, whole blood (1 mL) was added in direct contact with the scaffolds. Plates were incubated at 37 °C with gentle agitation for 30 min; then, scaffolds were re-weighed, and the tare weight was subtracted to obtain the mass of each thrombus. To assess fibrinogen adsorption, plasma was extracted from fresh whole blood by centrifugation at 180*g* for 15 min at room temperature, mixed 1:1 with fibrinogen conjugated with an Alexa Fluor 488 fluorescent label (cat. no. F13191, Thermo Fisher Scientific, Waltham, MA, USA), and then added to each well (1 mL) in direct contact with scaffolds. Plates were incubated at 37 °C with gentle agitation for 25 and 40 min, and representative images were taken at Ex./Em. 495/519 nm with a Zeiss Axio Scope.A1.

Cell Culture. Human fibroblasts were cultured in Corning T-75 flasks in Dulbecco's Modified Eagle Medium (D-MEM) supplemented with 10% (v/v) fetal bovine serum, 1% (v/v) L-glutamine, and 1% (v/v) penicillin/streptomycin at 37 °C, 5% CO_2. Cells were subcultured at 80% confluency using trypsin−EDTA as the dissociative agent. Cells were used for experimentation between passages 6−8.

Cell Attachment, Spreading, and Proliferation. Cell attachment, spreading, and proliferation assays were performed by seeding fibroblasts onto scaffolds in Corning 96-well, flat-bottom polystyrene culture plates. For cell attachment, 1×10^4 fibroblasts were seeded onto each scaffold ($n = 4$) and incubated for 1 h at 37 °C, 5% CO_2. The culture medium was then removed, scaffolds were washed with PBS three times to remove unattached cells, and the relative number of attached cells were quantified using alamarBlue Cell Viability Reagent (cat. no. DAL1025, Thermo Fisher Scientific, Waltham, MA, USA) according to the manufacturer's instructions. Briefly, cells were incubated in a 10% v/v alamarBlue reagent in culture medium for 2 h at 37 °C, 5% CO_2. The alamarBlue reagent was then transferred to a fresh 96-well plate, and fluorescent intensity was measured with a Texan M-1000 plate reader at Ex./Em. 460/480 nm. For cell proliferation, 5×10^3 fibroblasts were seeded onto scaffolds ($n = 4$) and incubated for 3, 5, and 7 days at 37 °C, 5% CO_2. The culture medium was refreshed every other day. At each time point, culture medium was removed, scaffolds were washed gently in PBS, and the alamarBlue assay was performed as described earlier. The fluorescence of experimental samples (Fe) was normalized to the blank (Fb, culture medium with alamarBlue reagent not exposed to cells) according to eq 3

$$\text{normalized fluorescence} = \frac{\text{Fe} - \text{Fb}}{\text{Fb}} \tag{3}$$

Cells in both attachment and proliferation assays were fixed, permeabilized, stained with rhodamine−phalloidin (for F-actin) and DAPI (for nuclei), and imaged at Ex./Em. 540/565 nm and 358/461 nm, respectively. Cell spreading was measured from F-actin stains on scaffolds used in cell attachment assays. The ImageJ freehand selection tool was used to outline and measure the area of individual cells (total $n \geq 70$). Overlapping cells and cells crossing the image edge were excluded as individual outlines could not be accurately identified.

Animal Husbandry and Graft Implantation. All animal surgical procedures were approved by the Sydney Local Heath District Animal Welfare Committee (protocol number 2017/015A) and conducted in accordance with the Australian Code of Practice for the Care and Use of Animals for Scientific Purpose. Five C57BL/6 mice were obtained from Animal BioResources (Moss Vale, NSW, Australia). Mice were housed in a self-ventilated OptiMice caging system with 12 h light/dark cycles at a constant temperature of 21 °C and ad libitum access to food and water.

Scaffolds were subcutaneously implanted in the dorsal surface of mice ($n = 5$), as previously reported.[28] Anesthesia was induced and maintained with 3% isoflurane. The dorsal surface of each mouse was shaved, sterilized with betadine solution, and washed with sterile PBS. Four 15 mm incisions were made in the skin of each mouse to create four separate subcutaneous pockets. One sterile 6 mm biopsy punched scaffold was inserted into each incision such that each mouse had 4 implants, 1 of each condition—0, 20, 40, and 60% CS-*g*-PCL. Incisions were closed with 6-0 silk sutures (Ethicon, Raritan, NJ, USA). On day 14, mice were euthanized by cervical dislocation, and scaffolds with surrounding tissue (15 mm × 15 mm) were excised for histological analysis and immunofluorescent staining. No mice were sacrificed prematurely.

Histology and Immunofluorescence Staining. Excised scaffolds and tissue were fixed in 4% paraformaldehyde (PFA) for 4 h, dehydrated through an ethanol gradient, embedded in paraffin, and cross-sectioned at 5 μm. For histological analysis, sections were stained with hematoxylin and eosin (H&E). Immunofluorescence staining was performed following deparaffinization and antigen retrieval. Tissue sections were incubated with primary antibodies diluted 1:500 in BSA (5% w/v in PBS) overnight at 4 °C. Primary antibodies for macrophage polarization included: CD68 pan macrophage marker (1:500, ab125212), MHC Class II for M1 macrophages (1:500, ab180779), and CD206 for M2 macrophages (1:500,

https://doi.org/10.1021/acsbiomaterials.3c00553
ACS Biomater. Sci. Eng. XXXX, XXX, XXX−XXX

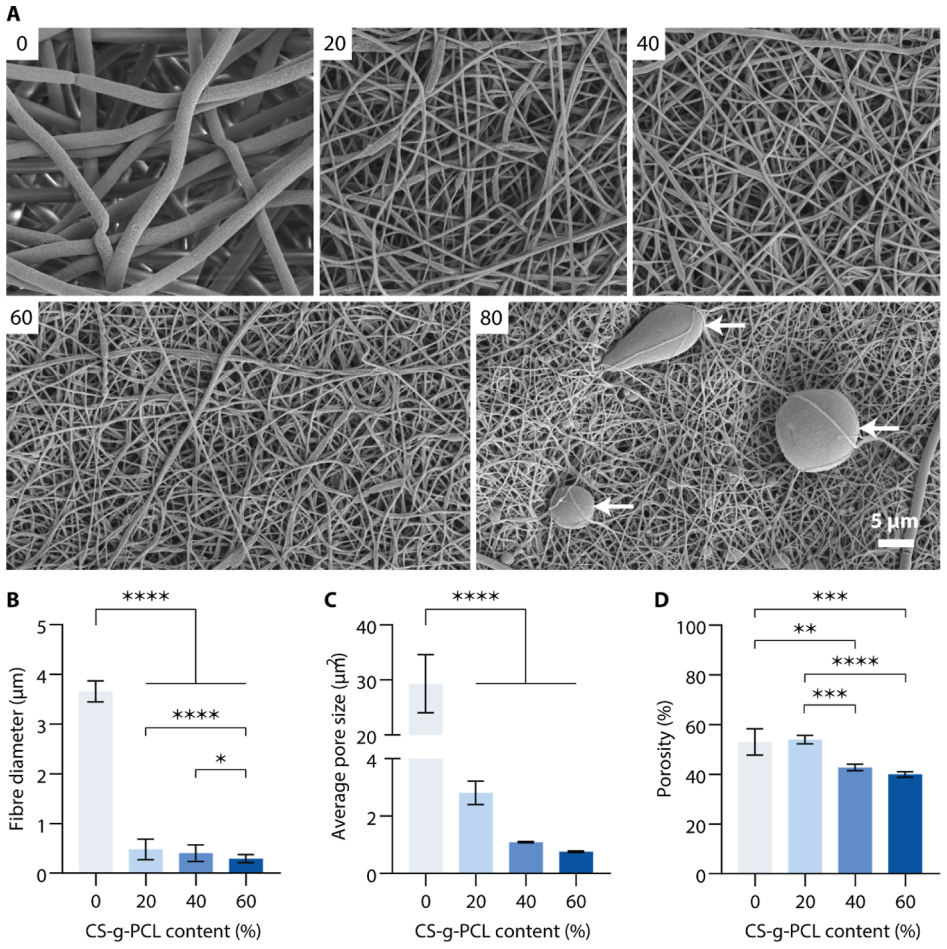

Figure 2. Structural characterization of electrospun chitosan-*graft*-PCL/PCL scaffolds. (A) Representative scanning electron micrographs of electrospun scaffolds. The number indicates the CS-*g*-PCL content (% w/w). 100% CS-*g*-PCL could not be electrospun. 80% CS-*g*-PCL was not investigated due to beading. White arrows indicate beading. (B) Fiber diameter of CS-*g*-PCL/PCL scaffolds (n = 10 fibers measured from each of n = 4 micrographs/blend). (C) Average size of pores measured at the surface plane (n = 4). (D) Porosity measured at the surface plane (n = 4). All data is mean ± SD. Significance indicated by *P < 0.05, **P < 0.01, ***P < 0.001, and ****P < 0.0001. CS-*g*-PCL, chitosan-*graft*-polycaprolactone.

ab64693). Primary antibodies for cytokines included: tumor necrosis factor (TNF)-α (1:500, ab6671), transforming growth factor (TGF)-β (1:500, ab92486), interleukin (IL)-10 (1:500, ab189392), and IL-1β (1:500, ab9722). The corresponding secondary antibodies in 1:500 dilutions used were Alexa Fluor 594 (ab150064) and Alexa Fluor 488 (ab150061). Cell nuclei were counterstained with DAPI mounting media (Fluoroshield, Sigma-Aldrich). Entire tissue sections were imaged on a Zeiss Axio Scan.Z1.

Histology Image Analysis. Quantitative measurements of histology images were made with ImageJ. The depth of cell infiltration, cell density, and capsule thickness were measured from H&E images. Cell infiltration depth was assessed using the line segment tool to measure the shortest distance from an infiltrated cell within the scaffold to the scaffold edge. For each replicate, 25 cells were chosen at random along the length of the scaffold, and infiltration depth was averaged. Infiltration depth for each replicate was then averaged for each blend (n = 5). Cell density within scaffolds and surrounding capsules was estimated using the particle analysis function. H&E images were color-deconvoluted (H&E) to isolate the hematoxylin color, representing cell nuclei. Particles with an area of 2.5−200 μm^2 were counted, irrespective of circularity, and presented as the number of cells per unit area (mm^2). The entire scaffold and capsule in each image were included (n = 5). Capsule thickness was determined using the line segment tool to measure the thickness of the capsule at 10 random locations in each replicate (n = 5 replicates). Macrophage infiltration was measured as the ratio of $CD68^+$ stained area within the capsule or scaffold to the area of the capsule or scaffold, respectively. Macrophage polarization was investigated by quantifying the ratio of MHC II^+:$CD68^+$ and $CD206^+$:$CD68^+$ stained areas for M1 and M2 macrophages, respectively, within the scaffold and capsule (n = 5).

Statistical Analysis. Statistical analyses were performed using GraphPad Prism 9 version 9.0.0 for Windows (GraphPad Software, San Diego, California USA). Values are mean ± SD. Statistical difference was determined using Student's t-test (two-tailed) for two-mean data sets; one-way analysis of variance (ANOVA) with post hoc Tukey's multiple comparison test for data sets with >2 means and one independent variable; and two-way ANOVA with post hoc Šidák's multiple comparison test for data sets with >2 means and two independent variables. A minimum sample size of three was used for calculating statistical significance. Values of P < 0.05 were considered significant.

RESULTS

Structural Characterization of CS-*g*-PCL/PCL Scaffolds. To assess the influence of CS-*g*-PCL on the physical properties of electrospun PCL scaffolds, a range of CS-*g*-PCL/PCL blends were examined with SEM to observe scaffold architecture. Solutions of 100% CS-*g*-PCL were not successfully electrospun at this concentration, and without further additives, they were unable to form a stable spinning jet.

https://doi.org/10.1021/acsbiomaterials.3c00553
ACS Biomater. Sci. Eng. XXXX, XXX, XXX−XXX

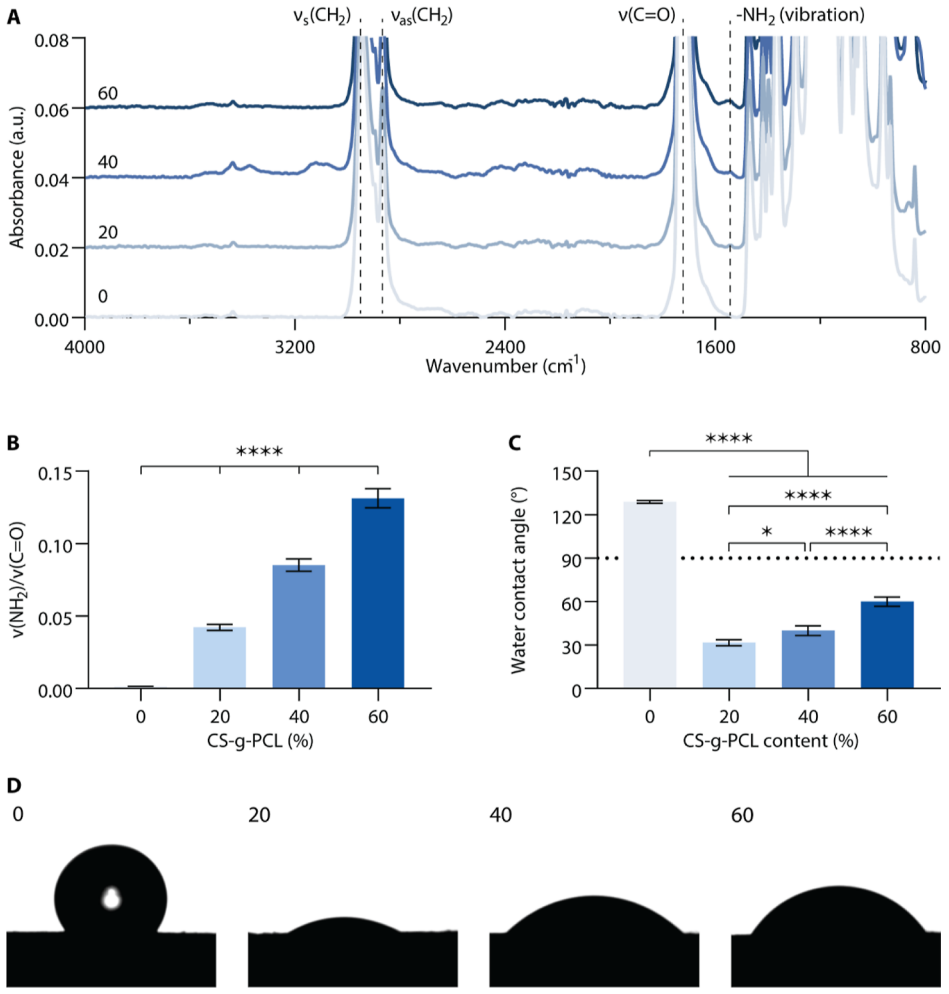

Figure 3. FTIR and water contact angle. (A) FTIR absorption spectra of electrospun CS-*g*-PCL/PCL blends with 0, 20, 40, and 60% CS-*g*-PCL. (B) Ratio of $\nu(NH_2)$ to $\nu(C{=}O)$ based on FTIR spectra, where $\nu(NH_2)$ indicates the presence of chitosan and $\nu(C{=}O)$ indicates the presence of PCL (n = 3). (C) Quantification of water contact angles (n = 3 droplets/blend). The dotted line indicates the threshold for hydrophilicity (<90°) and hydrophobicity (>90°). (D) Representative images of water contact angle testing. The number indicates the CS-*g*-PCL content (%). All data is mean ± SD. Significance is indicated by *P < 0.05 and ****P < 0.0001. CS-*g*-PCL, chitosan-*graft*-polycaprolactone.

Therefore, 100% CS-*g*-PCL was not investigated further. Increasing the CS-*g*-PCL content resulted in scaffolds with changes to multiple aspects of their architecture. Changes to solution concentration and flow rate for PCL only were unable to match these architectural changes, meaning that the addition of chitosan allowed the formation of thin fibers that we could not achieve with PCL alone (Supporting Information Figure S1). Our comparative analysis was therefore necessary between scaffolds with multi-faceted changes to their composition.

SEM micrographs showed that all scaffolds consisted of cylindrical fibers with random orientations (Figure 2A). Distinctive spherical-shaped beads were visible in 80% CS-*g*-PCL scaffolds, indicating inconsistent spinning, so this blend was also excluded from further investigation. PCL-only controls and 20, 40, and 60% CS-*g*-PCL scaffolds were carried forward. Higher CS-*g*-PCL content was generally associated with thinner fiber diameters (Figure 2B). Increasing the CS-*g*-PCL content from 0 to 20% significantly reduced the fiber diameter from 3.6 ± 0.21 μm to 0.48 ± 0.21 μm. Fibers within 40% CS-*g*-PCL scaffolds (0.40 ± 0.17 μm) were similar in diameter to 20% but significantly thinner within 60% CS-*g*-PCL scaffolds (0.30 ± 0.08 μm) compared to 20 and 40% CS-*g*-PCL scaffolds. The average pore size also decreased with the addition of CS-*g*-PCL (Figure 2C). Control PCL scaffolds had significantly larger pores than all other blends (29.33 ± 5.28 μm^2). Despite a decreasing trend, the pore sizes between scaffolds containing 20% (2.81 ± 0.41 μm^2), 40% (1.09 ± 0.03 μm^2), and 60% (0.76 ± 0.02 μm^2) CS-*g*-PCL were not statistically different. The porosity of PCL-only scaffolds (53.0 ± 5.3%) was similar to those containing 20% CS-*g*-PCL (54.0 ± 1.7%), but greater than those containing 40% (42.8 ± 1.3%) and 60% (40.0 ± 1.1%) CS-*g*-PCL (Figure 2D). Increasing the CS-*g*-PCL content also reduced overall scaffold thickness (Supporting Information Figure S2).

Physical and Mechanical Properties of CS-*g*-PCL/PCL Scaffolds. Infrared spectra of pure PCL and CS-*g*-PCL blends were acquired to study the chemical composition and confirm the incorporation of CS into the scaffolds (Figure 3A). All scaffolds featured absorption bands distinctive of PCL, including symmetric (~2940 cm^{-1}) and asymmetric (~2865 cm^{-1}) stretching vibrations of $-CH_2$ groups and a strong signature corresponding to vibrations of $-C{=}O$ bonds (~1720 cm^{-1}). The incorporation of CS in scaffolds electrospun with blends containing CS-*g*-PCL was confirmed by the presence of an absorption band centered around 1533

https://doi.org/10.1021/acsbiomaterials.3c00553
ACS Biomater. Sci. Eng. XXXX, XXX, XXX−XXX

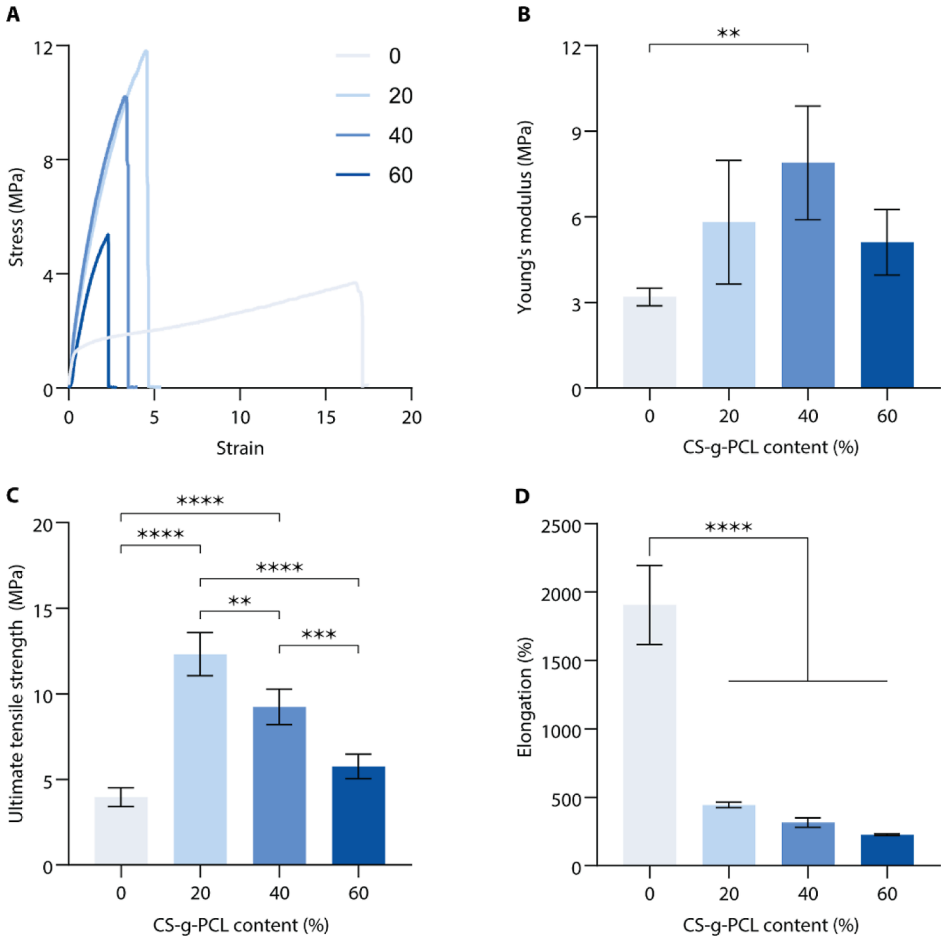

Figure 4. Uni-axial tensile properties of chitosan-*graft*-PCL/PCL. (A) Representative stress−strain curves of CS-*g*-PCL/PCL scaffolds under a strain rate of 10 mm/min. The legend denotes CS-*g*-PCL content (%). (B) Young's modulus of CS-*g*-PCL/PCL scaffolds. (C) Ultimate tensile strength of CS-*g*-PCL/PCL scaffolds. (D) Elongation of CS-*g*-PCL/PCL scaffolds at failure. In (B−D) data are mean ± SD of $n = 4$. Significance indicated by $^{**}P < 0.01$, $^{***}P < 0.001$, and $^{****}P < 0.0001$. CS-*g*-PCL, chitosan-*graft*-polycaprolactone.

cm^{-1}, corresponding to scissoring vibrations of $-NH_2$ bonds, which are not present in the chemical structure of pure PCL. FTIR measurements confirmed a dose-dependent increase of CS in scaffolds with the addition of CS-*g*-PCL, as measured by the ratio between $-NH_2$ and $-C{=}O$ absorption bands (Figure 3B).

Water contact angle, measured as biomaterial hydrophilicity, is an important determinant of biological responses. PCL had a WCA of 128.9 ± 0.9°, classifying it as hydrophobic, while all blends containing CS-*g*-PCL were hydrophilic (defined as a WCA <90°) (Figure 3C,D). Interestingly, the addition of 20% CS-*g*-PCL caused a dramatic reduction in WCA (31.6 ± 2.1°) compared to other blends containing CS-*g*-PCL (40.0 ± 3.4° and 59.9 ± 3.2°).

Uniaxial tensile properties were examined to assess the effect of chitosan content on biomechanical properties. Representative stress−strain curves are shown in Figure 4A. Scaffolds with greater CS-*g*-PCL content demonstrated some increase in stiffness, although this only reached significance for 40% CS-*g*-PCL (Figure 4B). Importantly, ultimate tensile strength was also increased by the presence of CS-*g*-PCL in all blends, with the highest value of for 20% CS-*g*-PCL (12.3 ± 1.3 MPa) and remaining significantly higher for 40% (Figure 4C). The greater overall strength did, however, significantly reduce elongation (Figure 4D).

Blood Compatibility of CS-*g*-PCL/PCL Scaffolds. The blood compatibility of CS-*g*-PCL scaffolds was assessed by static whole blood adhesion and fibrinogen adsorption. Thrombogenicity, measured by the mass of thrombus formation on scaffolds, varied depending on the CS-*g*-PCL content (Figure 5A). Thrombus formation was highest on scaffolds containing 20% CS-*g*-PCL (70.8 ± 7.3 mg), significantly greater than PCL (39.7 ± 3.9 mg, $P < 0.01$). Scaffolds containing 40% CS-*g*-PCL were comparable to PCL (40.3 ± 8.8 mg), while 60% CS-*g*-PCL scaffolds had the lowest mass of thrombus (17.5 ± 3.4 mg). These results are complemented by representative images of fibrinogen adsorption (Figure 5B), which indicate fibrinogen adsorption was greatest on 20% CS-*g*-PCL and least on 40 and 60% CS-*g*-PCL scaffolds.

Fibroblast Attachment, Spreading, and Proliferation. The cellular compatibility of CS-*g*-PCL/PCL scaffolds was determined by attachment, spreading, and proliferation assays with human fibroblast cells. Fibroblast attachment was increased 1.7−1.9 times by the addition of any amount of CS-*g*-PCL tested compared to PCL alone (Figure 6A,C). There was no difference in fibroblast attachment between scaffolds containing CS-*g*-PCL. Measurements of cell area revealed fibroblast spreading was significantly lower on PCL scaffolds (819 ± 373 μm^2) compared to all scaffolds containing CS-*g*-PCL (1074-1189 μm^2) (Figure 6A,D). There was no

https://doi.org/10.1021/acsbiomaterials.3c00553
ACS Biomater. Sci. Eng. XXXX, XXX, XXX−XXX

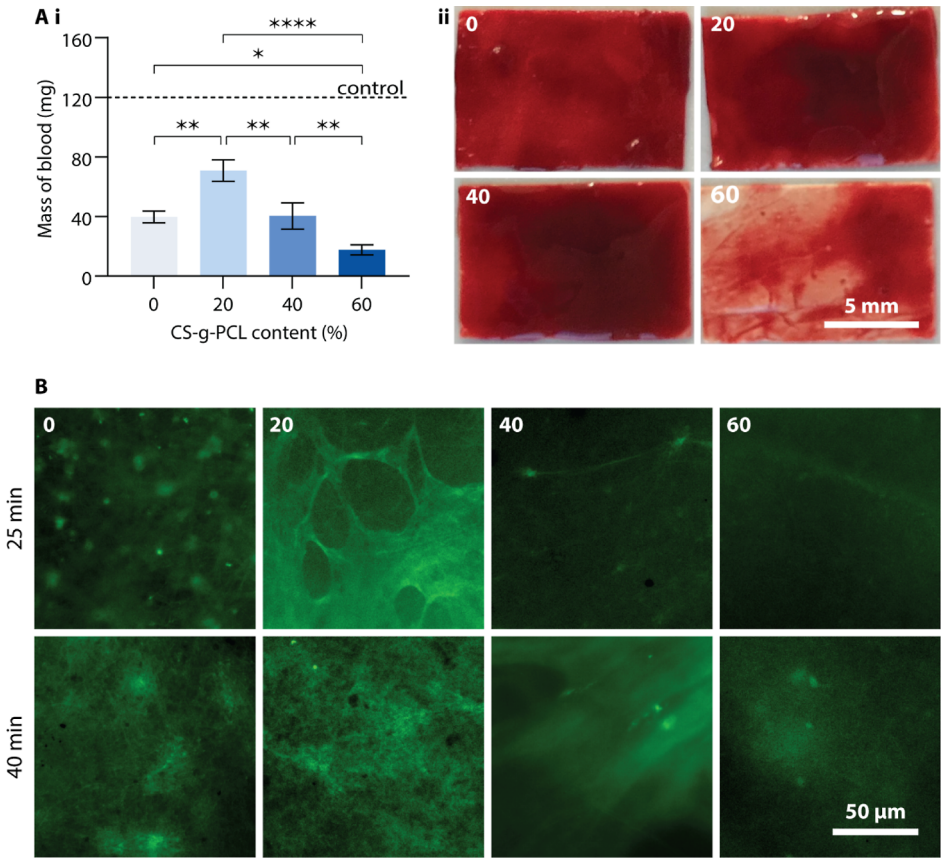

Figure 5. In vitro blood compatibility of chitosan-*graft*-PCL/PCL copolymer blends. (A) (i) Thrombogenicity of CS-*g*-PCL/PCL scaffolds measured by mass of thrombus formed after 30 min (n = 3). (ii) Representative images of scaffolds after whole blood clotting assay. The number indicates the CS-*g*-PCL content (%). (B) Representative images of fibrinogen adsorption to scaffolds after 25 and 40 min. Stainless steel was used as a positive reference material. Data are mean ± SD. Significance indicated by *P < 0.05, **P < 0.01, and ****P < 0.0001. CS-*g*-PCL, chitosan-*graft*-polycaprolactone.

difference in fibroblast spreading on scaffolds containing CS-*g*-PCL. Generally, cell proliferation increased steadily on all scaffolds during the incubation period (Figure 6B). After 7 days, cell density on 40 and 60% CS-*g*-PCL scaffolds was significantly higher compared to PCL controls (Figure 6E).

In Vivo Response to CS-*g*-PCL/PCL Scaffolds. Following favorable in vitro cellular and blood compatibility outcomes, we sought to investigate in vivo tissue and immune responses in a 14 day subcutaneous implantation model. H&E imaging was used to assess cellular infiltration into implanted scaffolds (Figure 7B). The depth of cellular infiltration was significantly greater in PCL-only scaffolds (83.1 ± 18.17 μm) compared to all scaffolds containing CS-*g*-PCL, with cells populating the full thickness of the scaffolds. Increasing CS-*g*-PCL content was associated with shallower cell infiltration. Scaffolds containing 20% CS-*g*-PCL showed mostly peripheral cellular infiltration (41.6 ± 7.4 μm) with few cells reaching the center of the scaffold, though still significantly greater compared to 40% (9.1 ± 5.5 μm) and 60% (5.1 ± 3.6 μm) scaffolds. For each blend, the majority of cells were located within the capsule surrounding the scaffold rather than within the scaffold itself (Figure 7C). The thickness of the capsule surrounding scaffolds was greatest for 20% CS-*g*-PCL, but the only significant difference was between 20 and 60% blends (Figure 7D). Higher magnification images demonstrating the delineation of the capsule boundary, supported by picrosirius red collagen staining, are shown in Supporting Information Figure S3.

Macrophage Response. Macrophage response was assessed by comparing infiltration into the capsule and scaffold, and quantifying the degree of polarization toward classically defined inflammatory (M1) and anti-inflammatory (M2) phenotypes (Figure 8A). After 14 days of subcutaneous implantation, macrophage ($CD68^+$) infiltration was inversely correlated with CS-*g*-PCL content (Figure 8B) within both the capsule and the scaffold, though differences were only significant within the scaffold. Polarization toward the M1 phenotype was not significantly different across all copolymer blends, with no discernible trend (Figure 8C). Similarly, there was no significant difference in M2 polarization, although there was a numerical increase in M2 macrophages present in scaffolds with a greater CS-*g*-PCL content (Figure 8D).

Cytokine Secretion. Next, we investigated pro-inflammatory (TNF-α and IL-1β) and anti-inflammatory (IL-10 and TGF-β) cytokine secretion by immunostaining to provide a more complete assessment of the immune response to CS-*g*-PCL/PCL copolymer blends. Increased CS-*g*-PCL content was associated with decreased secretion of pro-inflammatory cytokines (Figure 9). Compared with PCL, blends containing 60% CS-*g*-PCL showed significantly less secretion of TNF-α (2329 ± 1211 μm^2 vs 486 ± 336 μm^2, P < 0.01) and IL-1 β (20,133 ± 8650 μm^2 vs 3685 ± 1646 μm^2, P < 0.01). There

https://doi.org/10.1021/acsbiomaterials.3c00553
ACS Biomater. Sci. Eng. XXXX, XXX, XXX−XXX

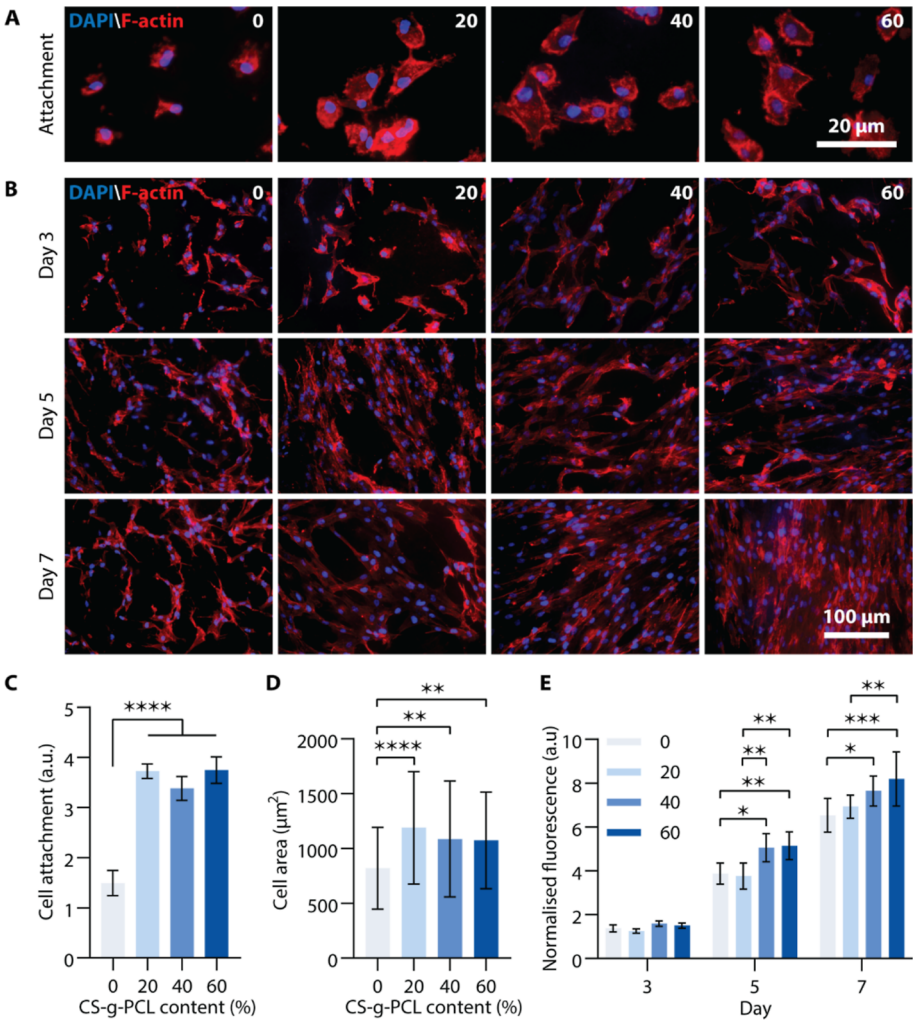

Figure 6. Human fibroblast attachment, spreading, and proliferation. (A) Images of DAPI/F-actin stains of fibroblast attachment to CS-*g*-PCL/PCL copolymer scaffolds after 1 h incubation. The numbers in the top left indicate the CS-*g*-PCL content (%). (B) Images of DAPI/F-actin stains of fibroblast proliferation on CS-*g*-PCL/PCL copolymer scaffolds after 3, 5, and 7 days. The number in top left indicates the CS-*g*-PCL content (%). (C) Quantification of fibroblast cell attachment to CS-*g*-PCL/PCL copolymer scaffolds by alamarBlue assay after 1 h of incubation (n = 4). Fluorescent intensity values are normalized to the blank and presented with arbitrary units (a.u.). (D) Quantification of cell spreading area on scaffolds measured 1 h after cell seeding ($n \geq 70$). (E) Quantification of fibroblast proliferation measured by the alamarBlue assay at days 3, 5, and 7 (n = 4). Fluorescent intensity values are normalized to the blank and presented with a.u. The legend indicates the CS-*g*-PCL content (%). All data are presented as mean ± SD. Significance indicated by *P < 0.05, **P < 0.01, ***P < 0.001, and ****P < 0.0001. CS-*g*- PCL, chitosan-*graft*-polycaprolactone.

was no significant difference in anti-inflammatory cytokine secretion or any clear trend across the blends (Figure 10).

DISCUSSION

PCL is widely used in tissue engineering applications due to its high mechanical strength, ease of manufacture, and demonstration that it is well tolerated in vivo.[8] However, PCL is hydrophobic and devoid of biological cues, leading to limited effectiveness in demanding biological applications such as small diameter vascular grafting.[5] One approach to overcome these limitations is the blending of PCL with well-characterized natural materials, such as chitosan, which are known to provide important biological signals and reduce hydrophobicity. Direct blending of PCL and chitosan (CS) for electrospinning has been previously documented to have these effects, but at the cost of reduced mechanical properties, resulting in brittle scaffolds with poor handling. This study aimed to characterize a CS-*g*-PCL copolymer which directly grafts PCL sidechains onto a CS backbone and overcomes these manufacturing limitations. The CS-*g*-PCL copolymer has been described previously in in vitro studies, but this is the first study to comprehensively define key physical and biological properties in vitro and in vivo.[31−35]

First, we generated a range of electrospun CS-*g*-PCL/PCL blends to determine the benefits of adding CS compared to PCL alone. Inherently, there are a number of variables involved in electrospinning that can impact final scaffold parameters, and we sought to keep as many of these fixed as possible.[36] Within the constraints of a single solvent (HFP), solution concentration (10% w/v), solution volume (4 mL), flow rate (1 mL/h), voltage (18 kV), and therefore spinning time, only a selection of blends were suitable for further study. Four blends of 0 (PCL-only control), 20, 40, and 60% CS-*g*-PCL content were selected, with higher concentrations of CS-*g*-PCL (80 and 100%) unsuitable for further investigation due to inefficient spinning in these conditions. PCL-only materials with matched

https://doi.org/10.1021/acsbiomaterials.3c00553
ACS Biomater. Sci. Eng. XXXX, XXX, XXX−XXX

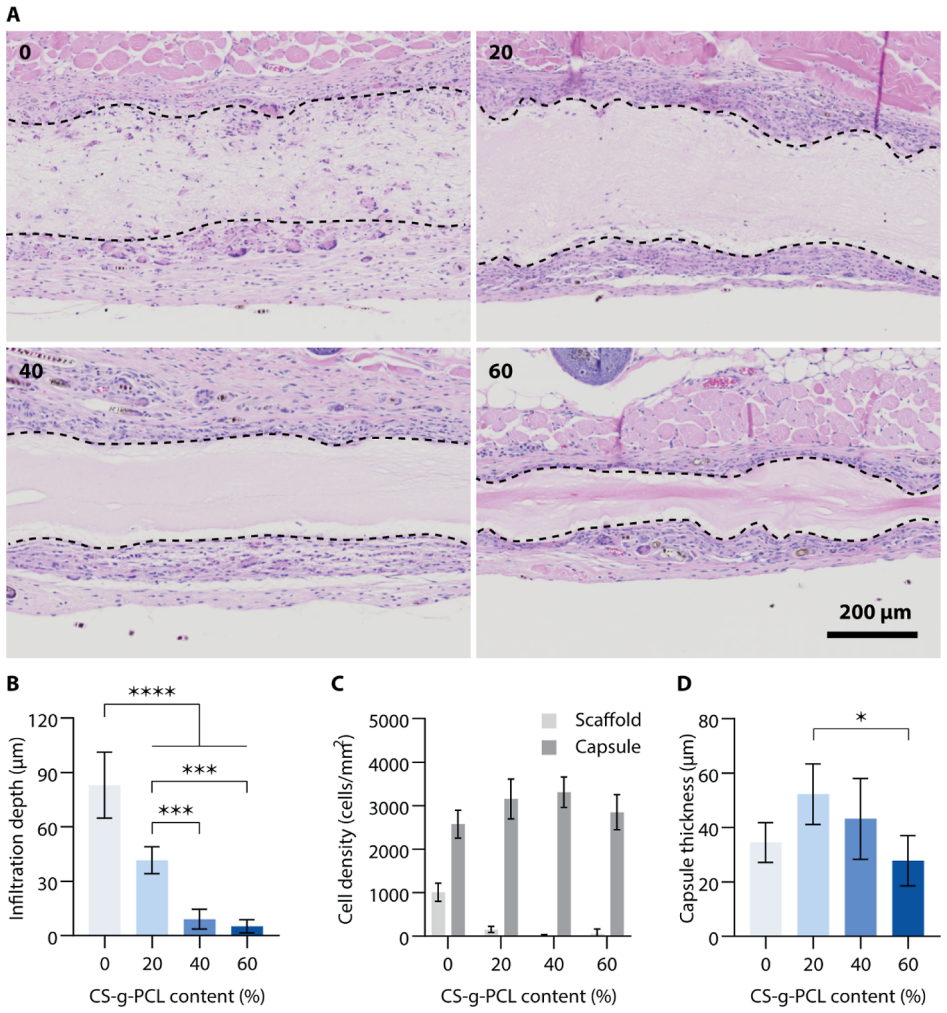

Figure 7. Tissue response to implanted chitosan-*graft*-PCL/PCL copolymer blends. (A) Representative hematoxylin and eosin (H&E) stains of scaffolds subcutaneously implanted in the dorsal surface of mice for 14 days. The number in top left indicates the CS-*g*-PCL content (%). A dotted black line indicates the edges of scaffolds. (B–D) Quantification of cell infiltration depth, cell density, and capsule thickness. All data presented as mean ± SD from $n = 5$. Significance indicated by $^{*}P < 0.05$, $^{***}P < 0.001$, and $^{****}P < 0.0001$. CS-*g*-PCL, chitosan-*graft*-polycaprolactone.

architecture could not be produced, even after exploring other solution concentrations, flow rates, and voltages.

Even with fixed production conditions, increasing proportions of CS-*g*-PCL resulted in scaffolds where multiple aspects of architecture and composition were changed. We first observed that increasing CS-*g*-PCL resulted in scaffolds with thinner fibers and reduced pore size and porosity, with an overall reduction in scaffold thickness. These changes in architecture were linked to scaffolds that were generally stiffer and stronger than PCL alone. The addition of chitosan likely resulted in thinner fiber diameters due to increased stretching of nanofibers caused by higher repulsion forces.[37] Further, the greater stiffness and reduced elongation observed with the addition of CS-*g*-PCL are likely due to higher crystallinity in blend fibers.[31] Changes to fiber size, arrangement, and crystallinity may all contribute to altered mechanical properties, consistent with other electrospun bio-synthetic hybrid materials containing chitosan, including chitosan/PCL and chitosan/polyvinyl alcohol (PVA).[38−40] Similar effects are also seen with other biological polymers, such as elastin, which, when combined with PCL, increased Young's modulus (35−120 MPa), tensile strength (10.6−18.1 MPa), and reduced elongation (55.0−25.3%).[41]

We also observed that the addition of CS-*g*-PCL decreased the water contact angle (WCA) of the scaffolds, indicating an increase in hydrophilicity. We acknowledge that there are multiple scaffold variables at play, contributing to this observation. The presence of polar amine and hydroxyl groups on the chitosan backbone was expected to enhance the hydrophilicity of CS-*g*-PCL/PCL scaffolds. However, a dose dependent relationship between the CS-*g*-PCL content and WCA did not arise, with a sharp decrease for the 20% scaffold. This may be partly explained by the distribution of chitosan within individual fibers. A similar study of electrospun CS-*g*-PCL/PCL scaffolds showed that the chitosan amine group is highly concentrated at the fiber surface, reaching a maximum at a relatively low CS-*g*-PCL content.[31] Further increases in the CS-*g*-PCL content would have little effect on WCA, so the increase in contact angles at a higher CS-*g*-PCL content may be ascribed to changes in other physical properties, such as roughness or pore size.[42] Taking into account the effect of chitosan distribution in individual fibers, the changes we observed between PCL alone (129°) and 20% CS-*g*-PCL (32°) were closely aligned with previous studies of PCL fiber dip-coating in CS-*g*-PCL (water contact angle reduced from

https://doi.org/10.1021/acsbiomaterials.3c00553
ACS Biomater. Sci. Eng. XXXX, XXX, XXX−XXX

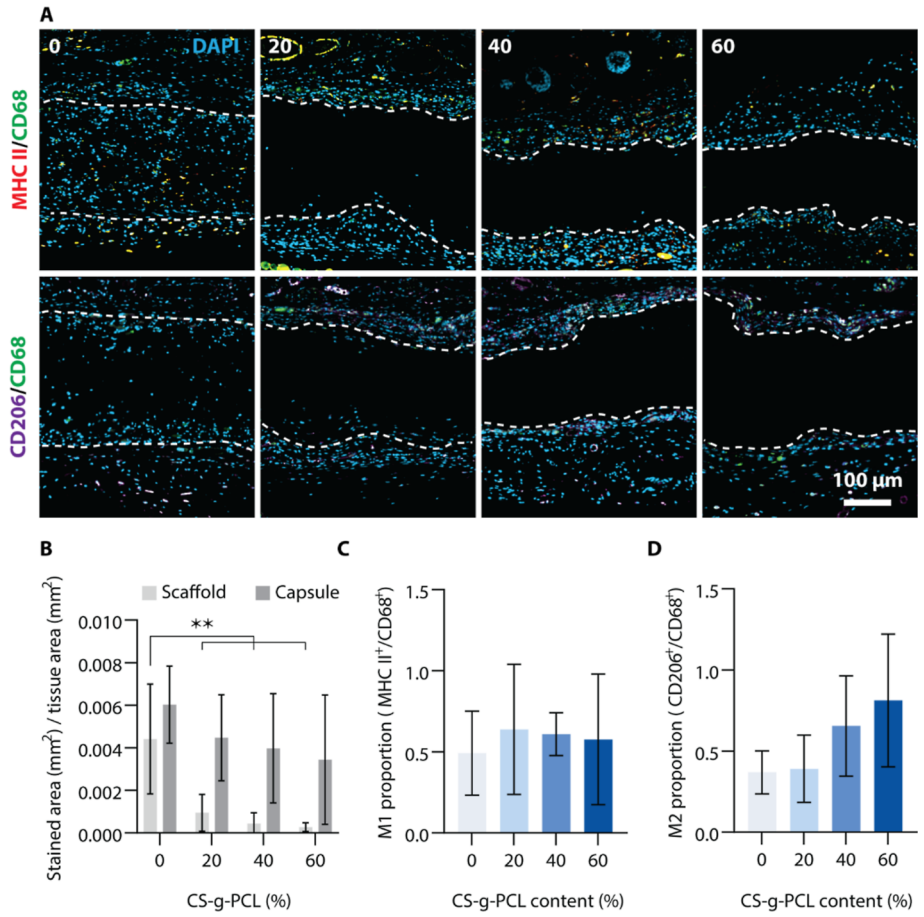

Figure 8. Macrophage polarization. (A) Immunohistochemical stains for M1 macrophages (MHC II/CD68) and M2 macrophages (CD206/CD68). The numbers in the upper left corners indicated the CS-*g*-PCL content (%). The dotted white line indicates the edges of scaffolds. Colored labels indicate the color of the stained marker. (B) Quantification of total macrophages ($CD68^+$) measured by stained area. (C) M1 macrophage polarization represented as a ratio of the MHC II^+ stained area to the $CD68^+$ stained area. (D) M2 macrophage polarization represented as a ratio of the $CD206^+$ stained area to the $CD68^+$ stained area. All data are presented as mean ± SD, $n = 5$. Significance indicated by $^{**}P < 0.01$. CS-*g*-PCL, chitosan-*graft*-polycaprolactone.

124° down to 34°), giving confidence that the CS-*g*-PCL component of the hybrid scaffolds plays a key role.[22]

Next, we examined the in vitro blood compatibility of the CS-*g*-PCL/PCL hybrid scaffolds using established static whole blood assays.[43] Measuring the weight of the thrombi formed, we observed at first a rise for 20% CS-*g*-PCL before a concentration-dependent decrease for higher concentrations. With multiple scaffold variables also influencing this result, it is likely that a combination of favorable features, including small fiber size and hydrophilicity, plays a role here. Scaffolds composed of very small fiber diameters (<1 μm) are known to be less thrombogenic than those with larger fiber diameters (3−5 μm) due to lower platelet adhesion and activation and less intense activation of the coagulation cascade.[44] Hydrophilicity also influences protein adsorption and induces enzyme conformational changes that expose binding or cleavage sites. Previous studies have demonstrated that under static conditions similar to ours, factor XIIa (FXIIa) activity is increased on hydrophilic materials compared to hydrophobic materials, contributing to greater fibrin fiber network volume and density.[45] This is supported by our fibrin network assembly results, showing the greatest fibrin amount on 20% CS-*g*-PCL scaffolds but reduced fibrin at higher concentrations. These promising trends need to be further assessed in more complex blood compatibility assays, such as under flow in a chandler loop, and ultimately in an appropriate in vivo model; however, 60% CS-*g*-PCL scaffolds clearly outperform the comparison materials here.[46]

To complete our in vitro characterization of the new scaffolds, we also assessed the attachment, spreading, and proliferation of human dermal fibroblasts. Our results showed that all scaffolds containing CS-*g*-PCL supported increased adhesion, spreading, and proliferation of fibroblasts at comparable rates, superior to PCL alone. Attachment and spreading results demonstrated a benefit in the presence of CS but no concentration-dependent effects. Again, this is likely due to the enrichment of chitosan amine groups at the fiber surface, reaching a maximum at relatively low concentrations of CS-*g*-PCL and consistent with prior studies of improved growth of human bone marrow mesenchymal stem cells on CS-*g*-PCL-coated scaffolds.[22,31] Other variables may also be relevant, with fiber size, hydrophilicity, and material mechanics all known to play a role in cell signaling behavior; however, fibroblasts are known to be somewhat less sensitive to substrate characteristics and are commonly used as a first assessment of overall cytocompatibility.[47−52] Most likely, the presence of natural CS in all the scaffolds provided sufficient biological cues for the fibroblasts to attach and spread compared to synthetic, hydrophobic PCL. Taken together,

https://doi.org/10.1021/acsbiomaterials.3c00553
ACS Biomater. Sci. Eng. XXXX, XXX, XXX−XXX

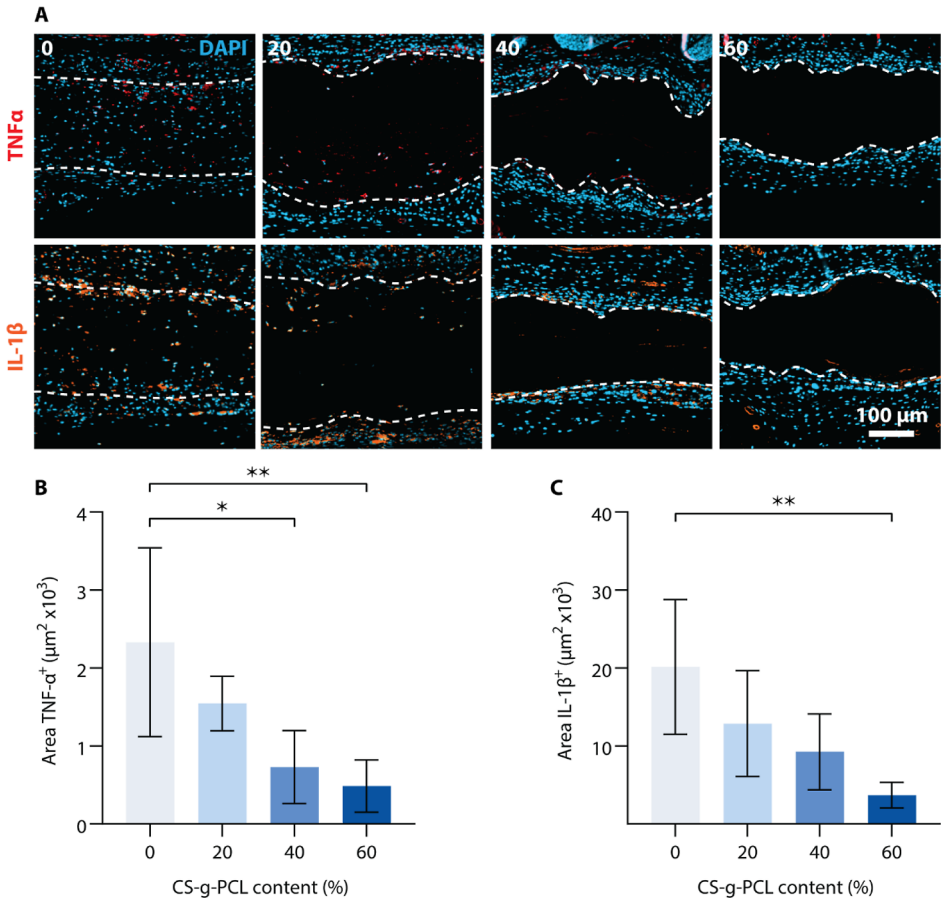

Figure 9. In vivo pro-inflammatory cytokine secretion. (A) Representative immunohistochemical stains of pro-inflammatory (TNF-α and IL-1β) cytokines. The numbers in the upper left corners indicated the CS-*g*-PCL content (%). The dotted white line indicates the edges of scaffolds. Colored labels indicate the color of the stained marker. (B, C) Quantification of TNF-α and IL-1β measured by the stained area. All data are presented as mean ± SD (n = 5). Significance is indicated by *P < 0.05 and **P < 0.01. CS-*g*-PCL, chitosan-*graft*-polycaprolactone.

our in vitro characterization justified further investigation of our scaffolds in vivo.

In this study, we used a mouse subcutaneous model, well established in our lab, as a high-throughput approach to characterizing the acute and sub-acute biological responses to new materials.[28,53] After 14 days of implantation, we observed several important differences for CS-*g*-PCL-containing blends compared to PCL alone. First, the infiltration of native cells inside the scaffolds was greatest in PCL alone, reducing as the CS-*g*-PCL content increased from 20 to 60%, with architecture likely the dominant cause. PCL-only scaffolds have the largest fiber diameter and greatest pore size, making them physically the easiest for cells to migrate into. The reduced scaffold thickness or increase in biological cues in higher CS-*g*-PCL content scaffolds ultimately had the least cell infiltration. All implants were surrounded by a cell-rich fibrous capsule of similar thickness, with only 60% CS-*g*-PCL, significantly less than 20% CS-*g*-PCL. H&E staining only provides an indication of the gross immune response, so we used immunostaining to further investigate differences between the scaffolds.

Macrophage-specific immunostaining revealed that they comprised only a small amount of the complete cell population, comparable to recent studies, with fewer total macrophages as CS-*g*-PCL content increased, reaching significance at 60%.[54] This outcome is perhaps most difficult to determine the origins of, as fiber size, porosity, mechanical properties, hydrophobicity, and the presence of biological cues from chitosan are all likely to have an influence.[55] Looking closer at macrophage polarization states, we observed no significant differences in M1 or M2 at this timepoint, potentially as these shifts are most commonly seen in the first days after implantation.[56] The fewer macrophages around the CS-*g*-PCL scaffolds did translate into important functional differences in the local inflammatory environment. Reduced macrophage burden correlated with a downregulation in the secretion of the classically pro-inflammatory cytokines TNF-α and IL-1β. These changes were significant for the 40% (TNF-α) and 60% (TNF-α and IL-1β) CS-*g*-PCL scaffolds. No changes in anti-inflammatory cytokines were observed. Overall, the in vivo results presented here substantiate previous in vitro reports on the anti-inflammatory action of chitosan. Pure chitosan films were found to drive downregulation of pro-inflammatory M1 macrophage markers CD68 and MHC II and lower secretion of TNF-α, while increasing IL-10 and TGF-β.[57] Further, CS-*g*-PCL films were found to reduce pro-inflammatory IL-12/23 secretion by M1 macrophages, while production of the M2 macrophage marker Arg1 was significantly increased.[34] Although further work is required to determine the mechanistic drivers influencing these immune response changes, it remains an important new observation that high CS-*g*-PCL content scaffolds are better tolerated in vivo.

https://doi.org/10.1021/acsbiomaterials.3c00553
ACS Biomater. Sci. Eng. XXXX, XXX, XXX−XXX

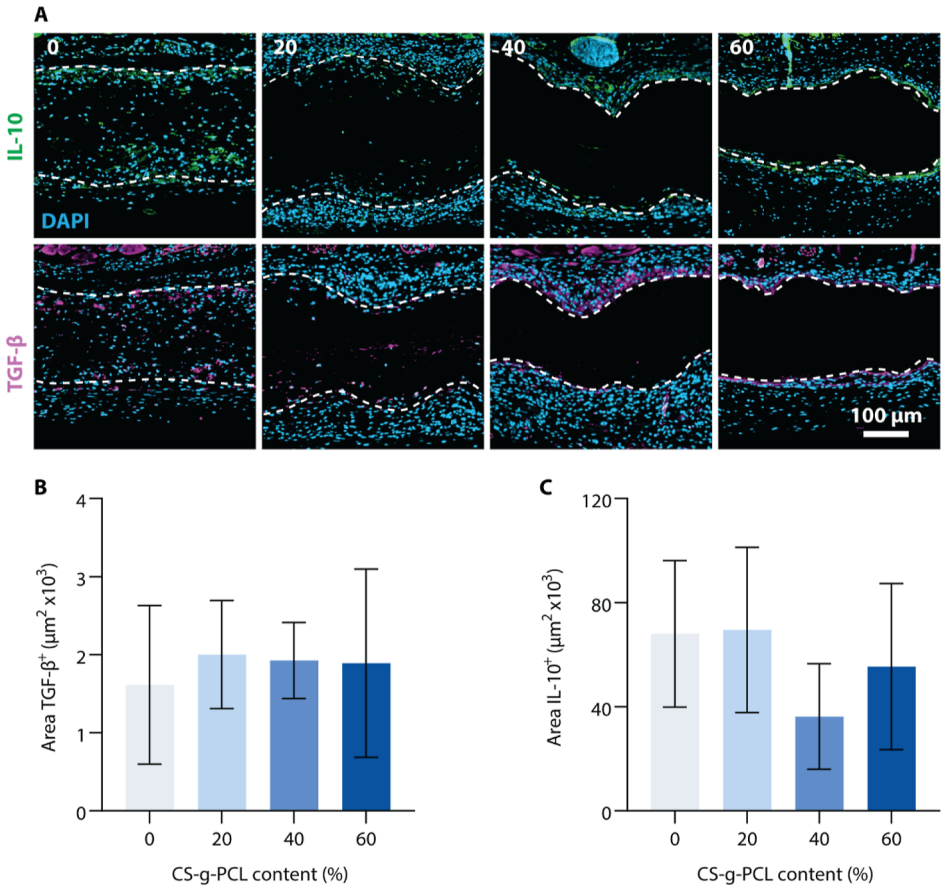

Figure 10. In vivo anti-inflammatory cytokine secretion. (A) Representative immunohistochemical stains of anti-inflammatory (IL-10 and TGF-β) cytokines. The numbers in the upper left corners indicated the CS-*g*-PCL content (%). The dotted white line indicates the edges of scaffolds. Colored labels indicate the color of the stained marker. (B,C) Quantification of TGF-β and IL-10 measured by the stained area. All data are presented as mean ± SD (n = 5). CS-*g*-PCL, chitosan-*graft*-polycaprolactone.

CONCLUSIONS

Taken together, our findings add significant data to the characterization of CS-*g*-PCL copolymers, including the first detailed in vivo response to implanted scaffolds, demonstrating a suite of favorable features. The addition of CS-*g*-PCL to electrospun PCL scaffolds leads to much thinner fibers than are achievable with PCL alone, increases hydrophilicity, improves blood contact, and increases cell attachment while increasing scaffold strength without compromising handling. In vivo, scaffolds with CS attract fewer macrophages, in turn reducing local inflammatory cytokines. These promising outcomes justify further work developing CS-*g*-PCL containing materials for specialty applications, such as small-diameter vascular grafts.

STUDY LIMITATIONS AND FUTURE DIRECTIONS

Our study characterizes new hybrid materials with valuable biological properties, potentially for vascular tissue engineering applications. However, we recognize that, inherent to our manufacturing process, several material variables are linked; as CS-*g*-PCL content increases, fiber diameter is reduced, contact angle, porosity, and mechanical behavior are all impacted. Undoubtedly, the addition of CS-*g*-PCL reduces fiber widths to diameters not achievable by electrospinning PCL alone, and higher-content CS-*g*-PCL materials are better tolerated in vivo. The improved performance is likely to have contributions from the materials chemistry as well as their architecture and mechanical properties. Looking ahead, further studies employing alternative manufacturing approaches, such as film pressing and additive manufacturing, are needed to produce materials with matched architecture/mechanics but changed CS-*g*-PCL content to uncouple the contribution of physical and biological cues.

ASSOCIATED CONTENT

Supporting Information

The Supporting Information is available free of charge at https://pubs.acs.org/doi/10.1021/acsbiomaterials.3c00553.

PCL fiber diameter optimization, scaffold thickness, and additional histology (PDF)

AUTHOR INFORMATION

Corresponding Author

Steven G. Wise − *School of Medical Sciences, Faculty of Health and Medicine, The University of Sydney, Camperdown, New South Wales 2006, Australia; Charles Perkins Centre and The University of Sydney Nano Institute, The University of Sydney, Camperdown, New South Wales 2006, Australia;* orcid.org/0000-0001-7964-819X; Phone: +61-2-86279458; Email: steven.wise@sydney.edu.au

https://doi.org/10.1021/acsbiomaterials.3c00553
ACS Biomater. Sci. Eng. XXXX, XXX, XXX−XXX

Authors

Matthew J. Moore − *School of Medical Sciences, Faculty of Health and Medicine, The University of Sydney, Camperdown, New South Wales 2006, Australia; Charles Perkins Centre, The University of Sydney, Camperdown, New South Wales 2006, Australia;* orcid.org/0000-0003-0536-6418

Yuen Ting Lam − *School of Medical Sciences, Faculty of Health and Medicine, The University of Sydney, Camperdown, New South Wales 2006, Australia; Charles Perkins Centre, The University of Sydney, Camperdown, New South Wales 2006, Australia*

Miguel Santos − *School of Medical Sciences, Faculty of Health and Medicine, The University of Sydney, Camperdown, New South Wales 2006, Australia; Charles Perkins Centre, The University of Sydney, Camperdown, New South Wales 2006, Australia*

Richard P. Tan − *School of Medical Sciences, Faculty of Health and Medicine, The University of Sydney, Camperdown, New South Wales 2006, Australia; Charles Perkins Centre, The University of Sydney, Camperdown, New South Wales 2006, Australia;* orcid.org/0000-0002-2670-2882

Nianji Yang − *School of Medical Sciences, Faculty of Health and Medicine, The University of Sydney, Camperdown, New South Wales 2006, Australia; Charles Perkins Centre, The University of Sydney, Camperdown, New South Wales 2006, Australia*

Juichien Hung − *School of Medical Sciences, Faculty of Health and Medicine, The University of Sydney, Camperdown, New South Wales 2006, Australia; Charles Perkins Centre, The University of Sydney, Camperdown, New South Wales 2006, Australia*

Zihao Li − *School of Chemistry, Australian Centre for NanoMedicine, UNSW, Sydney, New South Wales 2052, Australia;* orcid.org/0000-0002-1723-5047

Kristopher A. Kilian − *School of Chemistry, Australian Centre for NanoMedicine, UNSW, Sydney, New South Wales 2052, Australia;* orcid.org/0000-0002-8963-9796

Jelena Rnjak-Kovacina − *Graduate School of Biomedical Engineering, UNSW Australia, Sydney, New South Wales 2052, Australia;* orcid.org/0000-0001-6121-4676

Johannes B. Pitts − *Technische Universität Braunschweig, Institute for Technical Chemistry, Braunschweig 38106, Germany*

Henning Menzel − *Technische Universität Braunschweig, Institute for Technical Chemistry, Braunschweig 38106, Germany;* orcid.org/0000-0002-4915-7311

Complete contact information is available at: https://pubs.acs.org/10.1021/acsbiomaterials.3c00553

Author Contributions

S.G.W., H.M., and M.M. conceived and designed the study and experimental program. M.M., Y.T.L., M.S., R.P.T., N.Y., J.H., Z.L., and K.A.K. performed the experiments and data analysis. J.B.P. synthesized the CS-*g*-PCL biopolymer. M.M. wrote the manuscript with the assistance of S.G.W., J. R.-K., and H.M. All authors provided feedback on the final manuscript.

Notes

The authors declare no competing financial interest.

■ ACKNOWLEDGMENTS

This work was supported by the National Health and Medical Research Council (APP1162969, S.G.W. and J.R.K.) and the NSW Health Cardiovascular Capacity Building Grant (S.G.W. and J.R.K.) and received funding from the Sydney Local Health District (S.G.W.). S.G.W. is the recipient of a National Heart Foundation Future Leader Fellowship (105622). The authors acknowledge the facilities as well as scientific and technical assistance at Sydney Microscopy & Microanalysis, The University of Sydney. M.J.M. was supported by an Australian Government Research Training Program scholarship. H.M. and J.B.P. acknowledge funding by Deutsche Forschungsgemeinschaft (DFG) in the framework of the Research Unit FOR2180 "Graded Implants" AOBJ:650610.

■ REFERENCES

(1) Bartnikowski, M.; Dargaville, T. R.; Ivanovski, S.; Hutmacher, D. W. Degradation mechanisms of polycaprolactone in the context of chemistry, geometry and environment. *Prog. Polym. Sci.* **2019**, *96*, 1−20.

(2) Mondal, D.; Griffith, M.; Venkatraman, S. S. Polycaprolactone-based biomaterials for tissue engineering and drug delivery: Current scenario and challenges. *Int. J. Polym. Mater. Polym. Biomater.* **2016**, *65*, 255−265.

(3) Hernán Pérez De La Ossa, D.; Ligresti, A.; Gil-Alegre, M. E.; Aberturas, M. R.; Molpeceres, J.; Di Marzo, V.; Torres Suárez, A. I. Poly-ε-caprolactone microspheres as a drug delivery system for cannabinoid administration: Development, characterization and in vitro evaluation of their antitumoral efficacy. *J. Controlled Release* **2012**, *161*, 927−932.

(4) Janmohammadi, M.; Nourbakhsh, M. S. Electrospun polycaprolactone scaffolds for tissue engineering: A review. *Int. J. Polym. Mater. Polym. Biomater.* **2019**, *68*, 527−539.

(5) De Valence, S.; Tille, J.-C.; Mugnai, D.; Mrowczynski, W.; Gurny, R.; Möller, M.; Walpoth, B. H. Long term performance of polycaprolactone vascular grafts in a rat abdominal aorta replacement model. *Biomaterials* **2012**, *33*, 38−47.

(6) Mugnai, D.; Tille, J.-C.; Mrówczyński, W.; De Valence, S.; Montet, X.; Möller, M.; Walpoth, B. H. Experimental noninferiority trial of synthetic small-caliber biodegradable versus stable vascular grafts. *J. Thorac. Cardiovasc. Surg.* **2013**, *146*, 400−407.e1.

(7) Mrówczyński, W.; Mugnai, D.; De Valence, S.; Tille, J.-C.; Khabiri, E.; Cikirikcioglu, M.; Möller, M.; Walpoth, B. H. Porcine carotid artery replacement with biodegradable electrospun poly-e-caprolactone vascular prosthesis. *J. Vasc. Surg.* **2014**, *59*, 210−219.

(8) Woodruff, M. A.; Hutmacher, D. W. The return of a forgotten polymer—Polycaprolactone in the 21st century. *Prog. Polym. Sci.* **2010**, *35*, 1217−1256.

(9) Moore, M. J.; Tan, R. P.; Yang, N.; Rnjak-Kovacina, J.; Wise, S. G. Bioengineering artificial blood vessels from natural materials. *Trends Biotechnol.* **2022**, *40*, 693−707.

(10) Gomes, S.; Rodrigues, G.; Martins, G.; Henriques, C.; Silva, J. C. Evaluation of nanofibrous scaffolds obtained from blends of chitosan, gelatin and polycaprolactone for skin tissue engineering. *Int. J. Biol. Macromol.* **2017**, *102*, 1174−1185.

(11) Joyce, K.; Fabra, G. T.; Bozkurt, Y.; Pandit, A. Bioactive potential of natural biomaterials: identification, retention and assessment of biological properties. *Signal Transduct. Targeted Ther.* **2021**, *6*, 122.

(12) Chung, Y.-C.; Chen, C.-Y. Antibacterial characteristics and activity of acid-soluble chitosan. *Bioresour. Technol.* **2008**, *99*, 2806−2814.

(13) Dai, T.; Tanaka, M.; Huang, Y. Y.; Hamblin, M. R. Chitosan preparations for wounds and burns: Antimicrobial and wound-healing effects. *Expert Rev. Anti-Infect. Ther.* **2011**, *9*, 857−879.

(14) Heinemann, C.; Heinemann, S.; Bernhardt, A.; Worch, H.; Hanke, T. Novel textile chitosan scaffolds promote spreading,

proliferation, and differentiation of osteoblasts. *Biomacromolecules* **2008**, *9*, 2913−2920.
(15) Ayaz, F.; Demir, D.; Bölgen, N. Differential anti-inflammatory properties of chitosan-based cryogel scaffolds depending on chitosan/gelatin ratio. *Artif. Cells, Nanomed. Biotechnol.* **2021**, *49*, 682−690.
(16) Tomihata, K.; Ikada, Y. In vitro and in vivo degradation of films of chitin and its deacetylated derivatives. *Biomaterials* **1997**, *18*, 567−575.
(17) Bagheri-Khoulenjani, S.; Taghizadeh, S. M.; Mirzadeh, H. An investigation on the short-term biodegradability of chitosan with various molecular weights and degrees of deacetylation. *Carbohydr. Polym.* **2009**, *78*, 773−778.
(18) Custódio, C. A.; Alves, C. M.; Reis, R. L.; Mano, J. F. Immobilization of fibronectin in chitosan substrates improves cell adhesion and proliferation. *J. Tissue Eng. Regener. Med.* **2010**, *4*, 316−323.
(19) Liu, L.; Li, Y.; Liu, H.; Fang, Y. Synthesis and characterization of chitosan-graft-polycaprolactone copolymers. *Eur. Polym. J.* **2004**, *40*, 2739−2744.
(20) Chen, H.; Huang, J.; Yu, J.; Liu, S.; Gu, P. Electrospun chitosan-graft-poly (ε-caprolactone)/poly (ε-caprolactone) cationic nanofibrous mats as potential scaffolds for skin tissue engineering. *Int. J. Biol. Macromol.* **2011**, *48*, 13−19.
(21) Jing, X.; Mi, H.-Y.; Wang, X.-C.; Peng, X.-F.; Turng, L.-S. Shish-kebab-structured poly(ε-caprolactone) nanofibers hierarchically decorated with chitosan−poly(ε-caprolactone) copolymers for bone tissue engineering. *ACS Appl. Mater. Interfaces* **2015**, *7*, 6955−6965.
(22) De Cassan, D.; Sydow, S.; Schmidt, N.; Behrens, P.; Roger, Y.; Hoffmann, A.; Hoheisel, A. L.; Glasmacher, B.; Hansch, R.; Menzel, H. Attachment of nanoparticulate drug-release systems on poly-(epsilon-caprolactone) nanofibers via a graft polymer as interlayer. *Colloids Surf., B* **2018**, *163*, 309−320.
(23) Shirzaei Sani, I.; Rezaei, M.; Baradar Khoshfetrat, A.; Razzaghi, D. Preparation and characterization of polycaprolactone/chitosan-g-polycaprolactone/hydroxyapatite electrospun nanocomposite scaffolds for bone tissue engineering. *Int. J. Biol. Macromol.* **2021**, *182*, 1638−1649.
(24) Chatzinikolaidou, M.; Kaliva, M.; Batsali, A.; Pontikoglou, C.; Vamvakaki, M. Wharton's jelly mesenchymal stem cell response on chitosan-graft-poly (epsilon -caprolactone) copolymer for myocardium tissue engineering. *Curr. Pharm. Des.* **2014**, *20*, 2030−2039.
(25) Chen, H.; Fan, X.; Xia, J.; Chen, P.; Zhou, X.; Huang, J.; Yu, J.; Gu, P. Electrospun chitosan-graft-poly (ε-caprolactone)/poly (ε-caprolactone) nanofibrous scaffolds for retinal tissue engineering. *Int. J. Nanomed.* **2011**, *6*, 453−461.
(26) Reifenrath, J.; Wellmann, M.; Kempfert, M.; Angrisani, N.; Welke, B.; Gniesmer, S.; Kampmann, A.; Menzel, H.; Willbold, E. TGF-beta loaded electrospun polycaprolactone fibre scaffolds for rotator cuff tear repair: An in vivo study in rats. *Int. J. Mol. Sci.* **2020**, *21*, 1046.
(27) Gniesmer, S.; Brehm, R.; Hoffmann, A.; Cassan, D.; Menzel, H.; Hoheisel, A. L.; Glasmacher, B.; Willbold, E.; Reifenrath, J.; Wellmann, M.; Ludwig, N.; Tavassol, F.; Zimmerer, R.; Gellrich, N. C.; Kampmann, A. In vivo analysis of vascularization and biocompatibility of electrospun polycaprolactone fibre mats in the rat femur chamber. *J. Tissue Eng. Regener. Med.* **2019**, *13*, 1190−1202.
(28) Yang, N.; Moore, M. J.; Michael, P. L.; Santos, M.; Lam, Y. T.; Bao, S.; Ng, M. K. C.; Rnjak-Kovacina, J.; Tan, R. P.; Wise, S. G. Silk fibroin scaffold architecture regulates inflammatory responses and engraftment of bone marrow-mononuclear cells. *Adv. Healthcare Mater.* **2021**, *10*, 2100615.
(29) Ho, J. P. Y.; Nosworthy, N. J.; Bilek, M. M. M.; Gan, B. K.; Mckenzie, D. R.; Chu, P. K.; Dos Remedios, C. G. Plasma-treated polyethylene surfaces for improved binding of active protein. *Plasma Processes Polym.* **2007**, *4*, 583−590.
(30) Law, K.-Y. Definitions for hydrophilicity, hydrophobicity, and superhydrophobicity: Getting the basics right. *J. Phys. Chem. Lett.* **2014**, *5*, 686−688.
(31) Cassan, D.; Becker, A.; Glasmacher, B.; Roger, Y.; Hoffmann, A.; Gengenbach, T. R.; Easton, C. D.; Hansch, R.; Menzel, H. Blending chitosan-g-poly(caprolactone) with poly(caprolactone) by electrospinning to produce functional fiber mats for tissue engineering applications. *J. Appl. Polym. Sci.* **2020**, *137*, 48650.
(32) Xu, Y. J.; Liu, B.; Zou, L. M.; Sun, C. K.; Li, W. G. Preparation and characterization of PLLA/chitosan-graft-poly (epsilon-caprolactone) (CS-g-PCL) composite fibrous mats: the microstructure, performance and proliferation assessment. *Int. J. Biol. Macromol.* **2020**, *162*, 320−332.
(33) Georgopoulou, A.; Kaliva, M.; Vamvakaki, M.; Chatzinikolaidou, M. Osteogenic potential of pre-osteoblastic cells on a chitosan-graft-polycaprolactone copolymer. *Materials* **2018**, *11*, 490.
(34) Papadimitriou, L.; Kaliva, M.; Vamvakaki, M.; Chatzinikolaidou, M. Immunomodulatory potential of chitosan-graft-poly(epsilon-caprolactone) copolymers toward the polarization of bone-marrow-derived macrophages. *ACS Biomater. Sci. Eng.* **2017**, *3*, 1341−1349.
(35) Wiens, M.; Elkhooly, T. A.; Schroder, H. C.; Mohamed, T. H. A.; Muller, W. E. G. Characterization and osteogenic activity of a silicatein/biosilica-coated chitosan-graft-polycaprolactone. *Acta Biomater.* **2014**, *10*, 4456−4464.
(36) Li, D.; Xia, Y. N. Electrospinning of nanofibers: Reinventing the wheel? *Adv. Mater.* **2004**, *16*, 1151−1170.
(37) Antaby, E.; Klinkhammer, K.; Sabantina, L. Electrospinning of chitosan for antibacterial applications—current trends. *Appl. Sci.* **2021**, *11*, 11937.
(38) Mahoney, C.; Conklin, D.; Waterman, J.; Sankar, J.; Bhattarai, N. Electrospun nanofibers of poly(ε-caprolactone)/depolymerized chitosan for respiratory tissue engineering applications. *J. Biomater. Sci., Polym. Ed.* **2016**, *27*, 611−625.
(39) Oviedo, M.; Montoya, Y.; Agudelo, W.; García-García, A.; Bustamante, J. Effect of molecular weight and nanoarchitecture of chitosan and polycaprolactone electrospun membranes on physicochemical and hemocompatible properties for possible wound dressing. *Polymers* **2021**, *13*, 4320.
(40) Koosha, M.; Mirzadeh, H. Electrospinning, mechanical properties, and cell behavior study of chitosan/PVA nanofibers. *J. Biomed. Mater. Res., Part A* **2015**, *103*, 3081−3093.
(41) Perez-Puyana, V.; Villanueva, P.; Jiménez-Rosado, M.; De La Portilla, F.; Romero, A. Incorporation of elastin to improve polycaprolactone-based scaffolds for skeletal muscle via electrospinning. *Polymers* **2021**, *13*, 1501.
(42) Szewczyk, P. K.; Ura, D. P.; Metwally, S.; Knapczyk-Korczak, J.; Gajek, M.; Marzec, M. M.; Bernasik, A.; Stachewicz, U. Roughness and fiber fraction dominated wetting of electrospun fiber-based porous meshes. *Polymers* **2018**, *11*, 34.
(43) Waterhouse, A.; Yin, Y.; Wise, S. G.; Bax, D. V.; Mckenzie, D. R.; Bilek, M. M. M.; Weiss, A. S.; Ng, M. K. C. The immobilization of recombinant human tropoelastin on metals using a plasma-activated coating to improve the biocompatibility of coronary stents. *Biomaterials* **2010**, *31*, 8332−8340.
(44) Milleret, V.; Hefti, T.; Hall, H.; Vogel, V.; Eberli, D. Influence of the fiber diameter and surface roughness of electrospun vascular grafts on blood activation. *Acta Biomater.* **2012**, *8*, 4349−4356.
(45) Ruhoff, A. M.; Hong, J. K.; Gao, L.; Singh, J.; Tran, C.; Mackie, G.; Waterhouse, A. Biomaterial wettability affects fibrin clot structure and fibrinolysis. *Adv. Healthcare Mater.* **2021**, *10*, 2100988.
(46) Hong, J. K.; Gao, L.; Singh, J.; Goh, T.; Ruhoff, A. M.; Neto, C.; Waterhouse, A. Evaluating medical device and material thrombosis under flow: Current and emerging technologies. *Biomater. Sci.* **2020**, *8*, 5824−5845.
(47) Badami, A. S.; Kreke, M. R.; Thompson, M. S.; Riffle, J. S.; Goldstein, A. S. Effect of fiber diameter on spreading, proliferation, and differentiation of osteoblastic cells on electrospun poly(lactic acid) substrates. *Biomaterials* **2006**, *27*, 596−606.
(48) Kim, S. H.; Ha, H. J.; Ko, Y. K.; Yoon, S. J.; Rhee, J. M.; Kim, M. S.; Lee, H. B.; Khang, G. Correlation of proliferation, morphology

https://doi.org/10.1021/acsbiomaterials.3c00553
ACS Biomater. Sci. Eng. XXXX, XXX, XXX−XXX

and biological responses of fibroblasts on LDPE with different surface wettability. *J. Biomater. Sci., Polym. Ed.* **2007**, *18*, 609−622.
(49) Chen, X. y.; Tu, Y.; Jiang, X. f.; Yang, K.; Yang, X. q.; Liu, Y. f.; Cheng, Y. c. Elastic modulus affects the growth and differentiation of neural stem cells. *Neural Regener. Res.* **2015**, *10*, 1523−1527.
(50) Duan, B.; Wu, L.; Yuan, X.; Hu, Z.; Li, X.; Zhang, Y.; Yao, K.; Wang, M. Hybrid nanofibrous membranes of PLGA/chitosan fabricated via an electrospinning array. *J. Biomed. Mater. Res., Part A* **2007**, *83A*, 868−878.
(51) Wu, L.; Li, H.; Li, S.; Li, X.; Yuan, X.; Li, X.; Zhang, Y. Composite fibrous membranes of PLGA and chitosan prepared by coelectrospinning and coaxial electrospinning. *J. Biomed. Mater. Res., Part A* **2010**, *92*, 563−574.
(52) Koosha, M.; Raoufi, M.; Moravvej, H. One-pot reactive electrospinning of chitosan/PVA hydrogel nanofibers reinforced by halloysite nanotubes with enhanced fibroblast cell attachment for skin tissue regeneration. *Colloids Surf., B* **2019**, *179*, 270−279.
(53) Tan, R. P.; Chan, A. H. P.; Lennartsson, K.; Miravet, M. M.; Lee, B. S. L.; Rnjak-Kovacina, J.; Clayton, Z. E.; Cooke, J. P.; Ng, M. K. C.; Patel, S.; Wise, S. G. Integration of induced pluripotent stem cell-derived endothelial cells with polycaprolactone/gelatin-based electrospun scaffolds for enhanced therapeutic angiogenesis. *Stem Cell Res. Ther.* **2018**, *9*, 70.
(54) Gniesmer, S.; Brehm, R.; Hoffmann, A.; De Cassan, D.; Menzel, H.; Hoheisel, A. L.; Glasmacher, B.; Willbold, E.; Reifenrath, J.; Ludwig, N.; Zimmerer, R.; Tavassol, F.; Gellrich, N. C.; Kampmann, A. Vascularization and biocompatibility of poly-(epsilon-caprolactone) fiber mats for rotator cuff tear repair. *PLoS One* **2020**, *15*, No. e0227563.
(55) Huyer, L. D.; Pascual-Gil, S.; Wang, Y.; Mandla, S.; Yee, B.; Radisic, M. Advanced strategies for modulation of the material−macrophage interface. *Adv. Funct. Mater.* **2020**, *30*, 1909331.
(56) Tan, R. P.; Chan, A. H. P.; Wei, S.; Santos, M.; Lee, B. S. L.; Filipe, E. C.; Akhavan, B.; Bilek, M. M.; Ng, M. K. C.; Xiao, Y.; Wise, S. G. Bioactive materials facilitating targeted local modulation of inflammation. *JACC: Basic Transl. Sci.* **2019**, *4*, 56−71.
(57) Oliveira, M. I.; Santos, S. G.; Oliveira, M. J.; Torres, A. L.; Barbosa, M. A. Chitosan drives anti-inflammatory macrophage polarisation and pro-inflammatory dendritic cell stimulation. *Eur. Cell. Mater.* **2012**, *24*, 136−153.

https://doi.org/10.1021/acsbiomaterials.3c00553
ACS Biomater. Sci. Eng. XXXX, XXX, XXX−XXX